JGR Planets

RESEARCH ARTICLE
10.1029/2020JE006499

Key Points:

- Regional left lateral shear could be responsible for forming the extensively deformed southern Leading Hemisphere Terrain
- Cratered blocks ("crater islands") on Enceladus could have formed through a process analogous to rotated clasts in shear zones on Earth
- The resurfacing event that formed the Leading Hemisphere Terrain (LHT) likely resulted from an elevated, South Polar Terrain (SPT)-like surface heat flux or high stresses (>1 MPa)

Correspondence to:
E. Leonard,
Erin.J.Leonard@jpl.nasa.gov

Citation:
Leonard, E. J., Yin, A., & Pappalardo, R. T. (2021). Forming relic cratered blocks: Left-lateral shear on Enceladus inferred from ice-shell deformation in the leading hemisphere. *Journal of Geophysical Research: Planets*, *126*, e2020JE006499. https://doi.org/10.1029/2020JE006499

Received 28 APR 2020
Accepted 16 DEC 2020

Author Contributions:
Conceptualization: E. J. Leonard
Formal analysis: E. J. Leonard
Investigation: E. J. Leonard
Methodology: E. J. Leonard, A. Yin
Supervision: A. Yin, R. T. Pappalardo
Writing – original draft: E. J. Leonard
Writing – review & editing: E. J. Leonard, A. Yin, R. T. Pappalardo

Forming Relic Cratered Blocks: Left-Lateral Shear on Enceladus Inferred From Ice-Shell Deformation in the Leading Hemisphere

E. J. Leonard[1,2], A. Yin[2], and R. T. Pappalardo[1]

[1]Jet Propulsion Laboratory, California Institute of Technology, Pasadena, CA, USA, [2]Department of Earth, Planetary, and Space Sciences, University of California, Los Angeles, CA, USA

Plain Language Summary The southern leading hemisphere of Enceladus contains a unique terrain characterized by blocks of older, cratered material surrounded by areas of younger ridged terrain. In order to, investigate how this terrain formed and its implications for the surface history of Enceladus, we create a structural map of the region, infer a formation mechanism, and apply a simplified analytical model. From the structural map, we draw a comparison to shear zones on Earth where coherent blocks are rotated while the material around them is deformed. This comparison allows us to calculate the heat flux required in the region at the time of formation. We find that the heat flux in the region of the cratered blocks may have been high when the terrain formed, similar to that in the South Polar Terrain of Enceladus today, or involved high stresses.

Abstract The Leading Hemisphere Terrain (LHT) of Enceladus has experienced distributed deformation expressed by the pervasive development of >100 km wide and >100s km long ductile strike-slip shear zones and sparsely distributed craters. Within the zones are locally preserved little-deformed semirigid blocks up to 10–20 km in size with surfaces dominated by impact craters. The edges of these relic blocks display ductile drag folds and smeared tails of rigid fragments, which are indicative of vertical-axis rotation associated with ductile strike-slip shear. Kinematic analysis requires the development of the LHT to have been driven mainly by toroidal flow of the ice-shell material. Additionally, the structural mapping quantifies the shear strain magnitude (2.8) and minimum strain rate (10^{-17} s^{-1}). If the observed deformation induced by tidal stress, the estimated ice-shell deformation requires a high heat flux (~0.13 W/m^2) and a thin brittle layer (~4 km) during the development of the LHT. However, the observed deformation may have formed under high stresses, exceeding 1 MPa and a heat flux similar to the current background observed today.

1. Introduction

Enceladus, a small icy satellite of Saturn with a diameter of ~500 km, displays a wide range of morphologic features that include active linear fractures emitting vapor jets, curvilinear ridges interpreted as folds, isolated zones of linear to curvilinear tensile cracks, and heavily cratered regions that have not experienced significant tectonic deformation in the past ~4 Ga (Figure 1; Crow-Willard & Pappalardo, 2015; Porco et al., 2006; Spencer et al., 2009; Spencer & Nimmo, 2013; Yin & Pappalardo, 2015). Recent research on the South Polar Terrain (SPT) of Enceladus has illuminated the mechanisms of active and recently active resurfacing processes (e.g., Barr & Preuss, 2010; Gall et al., 2017; Han et al., 2012; Mitri & Showman, 2008; Patthoff & Kattenhorn, 2011; Porco et al., 2014; Spitale et al., 2015; Yin et al., 2016; Yin & Pappalardo, 2015). However, it remains unclear if the same or similar processes have operated in the geologic past in currently inactive tectonically regions such as the Leading Hemisphere Terrain (LHT) and Trailing Hemisphere Terrain (THT; Figure 1; Crow-Willard & Pappalardo, 2015). Specifically, if the resurfacing processes that formed the LHT and THT were dominated by resurfacing mechanisms similar to those currently acting on the SPT, it would imply a cyclic evolution of the satellite possibly related to its orbital evolution around Saturn. Alternatively, if the resurfacing mechanisms differ drastically for the development of the three teutonized terrains on the icy satellite, a monotonic evolutionary trend possibly dictated by the history of the satellite could be deduced. It is with this motivation that we examine the deformation processes in the LHT where past geologic records are preserved and the implied mechanical and thermal states can be ascertained (e.g., Bland

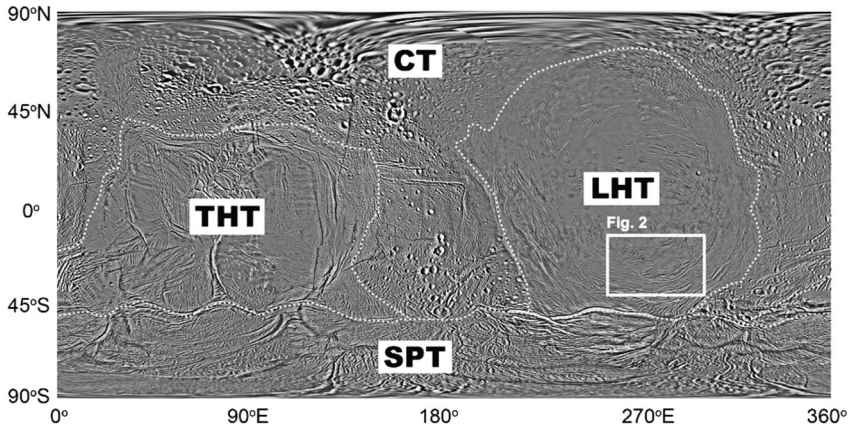

Figure 1. Global map of Enceladus with East positive coordinated in cylindrical projection and base map for geologic mapping (see text for the source of the image mosaic). The globe is divided into four general terrains after Crow-Willard and Pappalardo (2015): CT, Cratered Terrain; LHT, Leading Hemisphere Terrain; SPT, South Polar Terrain; THT, Trailing Hemisphere Terrain. The white box indicates the location of Figure 2.

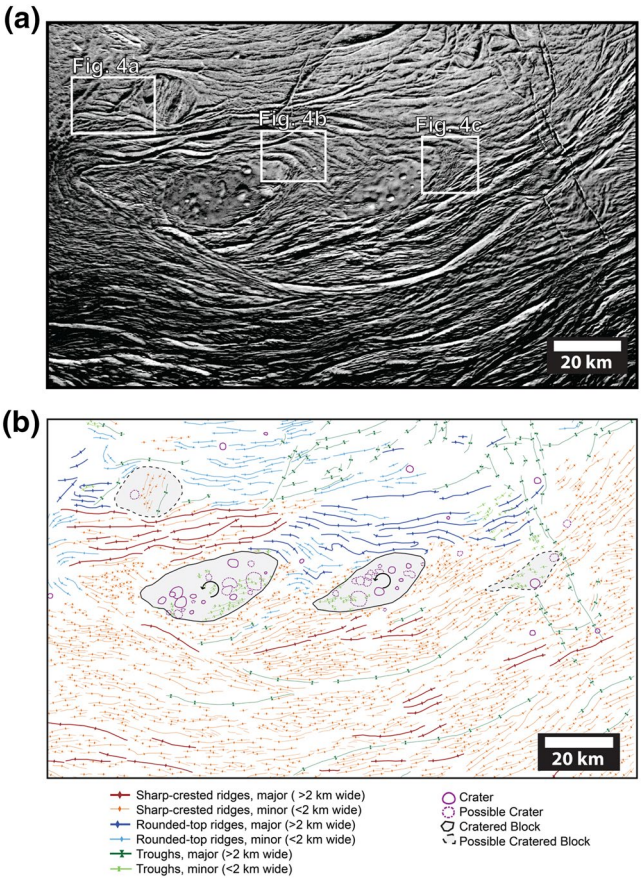

Figure 2. Image mosaic (a) of the region in the southern leading hemisphere of Enceladus that we map (centered around 30°S, 270°E). The location of this image is indicated by the white box in Figure 1 and the location of Figures 4a–4c are shown by the white boxes. A structural map (b) of region in Figure 2a highlighting the types of ridges and the extent of the relic cratered terrain. Note how the craters (purple) are concentrated on the relic cratered blocks.

et al., 2007, 2012, 2015; Lucchetti et al., 2017; Martin et al., 2017; Patthoff et al., 2015). The focus of this study is to show from detailed photogeologic mapping that the LHT (Figure 2a) has experienced distributed strike-slip ductile-shear deformation that occurred possibly as early as ~10 Ma based on crater count age estimates (Crow-Willard & Pappalardo, 2015; Spencer & Nimmo, 2013), immediately before the formation of the SPT in the past few million years (e.g. Porco et al., 2006).

As shown below, our mapping efforts establish the structural relationships around little-deformed blocks in ductilely sheared domains of the LHT; the heavily cratered blocks, referred to as "crater islands" by Crow-Willard and Pappalardo (2015), are most likely to be remnants of the adjacent Cratered Terrain (see Figure 1). Furthermore, we use the morphologic features around the relic cratered blocks, such as curvilinear ridges and troughs, to deduce the structural origin and kinematic development of the isolated cratered blocks (Section 3). When combined with constraints on stress magnitude, we will assess the past thermal state of the shear zone (Section 4), which we will then compare against the thermal regime across the currently active SPT (Section 5).

2. Data and Methods

The photogeologic mapping methods in this work are similar to the approach presented in Yin and Pappalardo (2015) and Leonard et al. (2018) that consists of two steps: (1) document the attributes of major morphological features, and (2) relate the morphologies and spatial distribution to plausible deformation mechanisms. The details of the data sources and the methods of mapping are briefly described below.

2.1. Data

We conducted the photogeologic mapping using a Cassini ISS mosaic product that is publicly available from United States Geological Survey (USGS) Astropedia (PDS Annex) at < astrogeology.uses.gov>. The global mosaic used in Figure 1 and the photogeologic mapping has a spatial resolution of ~100 m/pixel. The images used in this mosaic have a

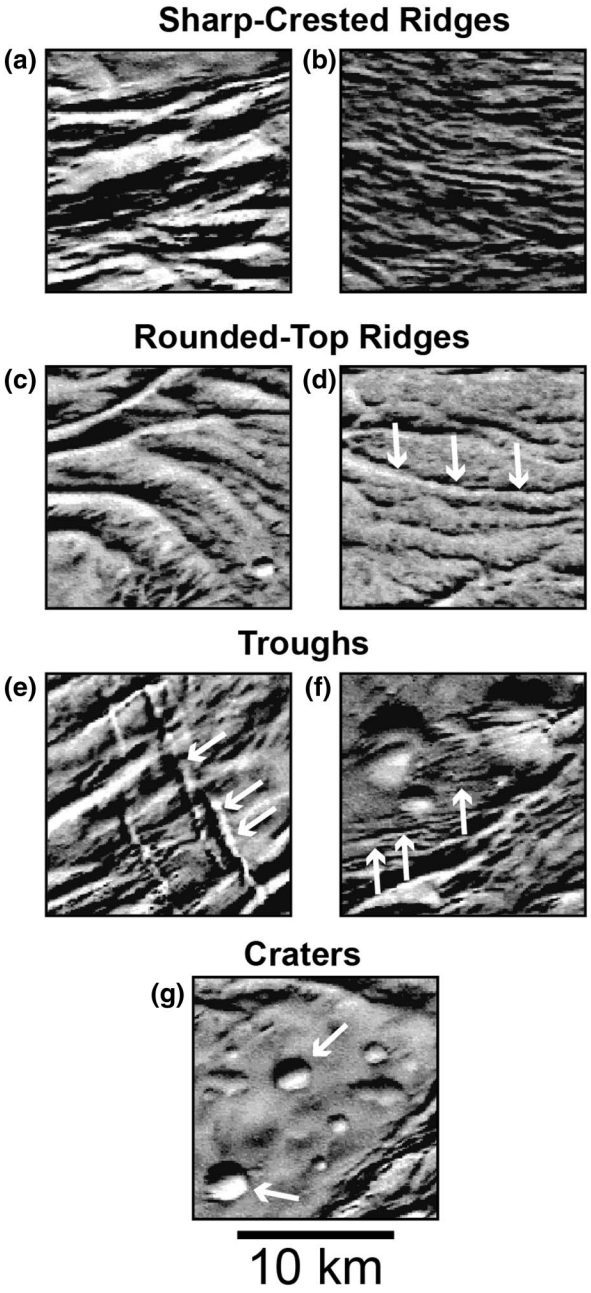

Figure 3. Index of structural units identified in Figure 2a, with type examples at a common scale for: major (a) and minor (b) Sharp-Crested Ridges, major (c) and minor (d) Rounded-Top Ridges, major (e) and minor (f) Troughs, and Craters (g). The unit descriptions are in Section 3.1.

spatial resolution between 50 m/pixel and 500 m/pixel and phase angles of < 120°, in order to allow for consistency across the global mosaic. The region where we conducted photogeologic mapping in this work (Figure 2a) is taken from a portion of the global mosaic.

2.2. Methods

We perform photogeologic mapping in the southern LHT region (Figure 2a) in order to investigate the unique "crater island" features identified by Crow-Willard and Pappalardo (2015) and analyze the structural origin and kinematic evolution of the region. The surface features are mapped based on the morphologic appearance interpretable from the satellite images such as cross-sectional geometry of ridges and troughs, surface textures, and landform shapes. We identify four main types of morphological units (Figure 3): (1) sharp-crest ridges (Figures 3a and 3b), (2) rounded-top ridges (Figures 3c and 3d), (3) troughs (Figures 3e and 3f), and (4) craters (Figure 3g). We further divide the ridge and trough units into "major" (>2 km in width) and "minor" (<2 km in width) subunits, which is an arbitrary division we set for categorization. We map any ridges >500 m in width and any craters with a diameter >1 km. See Section 3.1 for further description on the identified units. Assuming negligible erosion and deposition after the formation of the mapped morphologic features and assuming their origins were induced only by ice-shell deformation (see Section 3.2 for justification of these assumptions), we are able to use tectonic-geomorphology mapping methods (e.g., Burbank & Anderson, 2009) to relate the mapped landform features to assign a structural origin and the related kinematic evolution of a mapped feature (Table 1).

3. Structural Origin and Kinematic Evolution of Morphologic Features

In contrast to the development of parallel strike-slip and/or tensile fractures in the SPT (Patthoff & Kattenhorn, 2011; Porco et al., 2006; Yin & Pappalardo, 2015; Yin et al., 2016), the LHT of Enceladus is dominated by zones of narrow (<a few km in width) but long (>10s–100 s km) curvilinear ridges and troughs (Figures 1 and 2). The ridges—locally affected by sparsely distributed impact craters—merge, diverge, and surround semi-square and semi-elliptical blocks which are heavily cratered on the surface (Figure 2b). Through detailed morphologic mapping (Figure 2b), we can illuminate the structural relationships among curvilinear ridges/troughs and the little deformed relic blocks.

3.1. Morphologic Features

In mapping the southern LHT, we identify features and group them into categories based on morphology (e.g., apparent cross-sectional shape). The features and their associated morphologic characteristics are:

Sharp-crested ridges–quasilinear topographic high with a large length to width ratio that appear to be triangular in cross-section with asymmetric slopes. Major sharp-crested ridges are > 2 km in width (Figure 3a), whereas minor sharp-crested ridges are < 2 km wide (Figure 3b).

Table 1
Criteria for Identifying Various Types of Structures

	Tension cracks	Normal faults	Thrust faults	Circular folds	Box folds
Ridge morphology in cross section view	Commonly not associated with ridge formation.	Sharp ridge crest; one side of the ridge displays high-angle planar scarps.	Irregular ridge crests; symmetric or asymmetric slopes with the steep side above fault traces	Semi-circular, rounded ridge crest in cross section view; smooth and symmetric ridge slopes	Flat ridge tops; steep to vertical ridge flanks defining vertical fold limbs.
Trough morphology in cross section view	Steep walls, v-shaped in cross-section	Depression correlates with the extent of the bounding faults.	Irregular shaped basins induced by loading in the footwalls.	Troughs are synclinal folds with circular cross section geometry.	Steep walls bounded by draped limbs from flat fold top
Map-view geometry of mapped structures	Straight traces; can occur in parallel sets with even spacing	Relatively straight fault trace.	Highly curved, wavy fault traces. More discontinuous than fold traces	Both straight and curvilinear traces.	Both straight and curvilinear traces.
Interpretation of mapped morphologies	**Troughs (major and minor)**	**Sharp-crested ridges (major and minor)**	**Rounded-top ridges (major and minor)**	**Rounded-top ridges (major and minor)**	**Rounded-top ridges (major and minor)**

Notes: Modified from Yin and Pappalardo (2015). Interpretations associated with the mapping are in bold.

Rounded-top ridges–quasilinear topographic highs with a large length to width ratio that appear to be rounded to boxy in cross-section. The slopes of these ridges appear to be roughly symmetric. Major rounded-top ridges are > 2 km in width (Figure 3c), whereas minor rounded-top ridges are < 2 km wide (Figure 3d).

Troughs–quasilinear topographic lows with no associated ridge. These features have large length to width ratios and appear to be v-shaped in cross-section. Major troughs are > 2 km in width (Figure 3e), whereas minor troughs are < 2 km wide (Figure 3f).

Craters–roughly circular bowl-shaped depressions with a raised rim (Figure 3g). Craters are labeled as "possible" when the shape has been degraded or the topographic low is not apparent. The few craters mapped in the study area have diameters generally < 10 km and are concentrated exclusively on the surfaces of the relatively undeformed relic blocks.

Cratered Block–terrain made up of overlapping craters on a smooth background terrain. There are no ridges present on a cratered block. Cratered blocks are labeled as "possible" when there are few craters or ridges that trend in a significantly different direction than the surrounding terrain.

3.2. Structural Interpretations

Correlation between the observed morphologic features and their structural interpretations are listed in Table 1. The structural interpretations provided below assume that deposition and erosion have not altered significantly the surface shape of the mapped morphologic features (i.e., the shape of the observed morphological feature can still be related to its structural origin). This assumption is reasonable given the range of estimated sublimation rates of water ice in the Saturnian system in general and the low deposition rates for regions away from the SPT on Enceladus in particular (e.g., Leonard et al., 2018; Patterson et al., 2010; Prockter et al., 2000, 2002; Sieveka & Johnson, 1982; Spencer & Nimmo, 2013; Yin & Pappalardo, 2015). Research based on Cassini data indicates that space weathering, another possible modifier of the surface morphology, is also negligible at Enceladus (e.g., Paranicas et al., 2012). Additionally, we do not observe any evidence of postemplacement relaxation or downslope mass wasting, which could affect the original shape of mapped morphological features after their formation (e.g., Moore et al., 1999, 2009). Our structural analysis allows us to recognize the following key geologic features (Table 1): (1) tensile cracks that are expressed as linear and narrow troughs bounded by steep walls with a v-shaped cross-section geometry, (2) normal faults characterized by sharp-crested ridges flanked with asymmetric slopes; (3) thrust faults that are closely

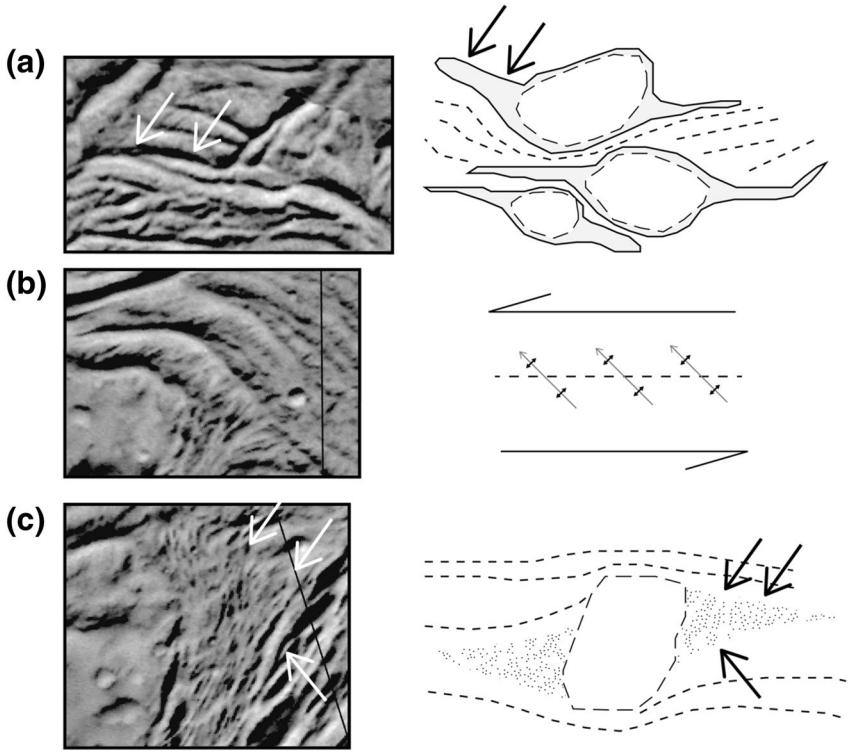

Figure 4. (a) Tail region of the rotated relic block (indicated by the white arrows), and schematic (right) traced and modified from Figure 3 in Passchier and Simpson (1986) indicating the formation of tails (indicated by the black arrows) on sigma clasts in centimeter scale samples on Earth; (b) compressional folds in proximity to the rotated block, and a schematic (right) depicting the expected orientation of contractional structures that form in a left-lateral shear zone—note the similar trend directions; (c) the strain shadow region (indicated by the white arrows) containing ridges that gradually change direction with proximity to the block, and a schematic (right) traced and modified from Figure 4 in Simpson and Schmid (1983) indicating where this strain shadow (indicated by the black arrows) forms with respect to a rotated clast. All of the images from Enceladus in this Figure are in a Mercator projection in order to allow for accurate angle measurements and comparisons.

associated with irregular or discontinuous ridges and have both linear to curvilinear traces, and (4) folds that are ridges with either circular or box-like cross-section geometry.

3.3. Kinematic Interpretations

Structural mapping (Figure 2b) suggests that the morphological features, dominated by curvilinear ridges and troughs, were generated during a single episode of deformation with the exception for the later north-trending tensile cracks on the east side of the mapped area. The single episode of deformation is indicated by the absence of offsets and cross-cutting relationships of the geologic structures that have different orientations and morphological expressions (see Section 5.1 for further discussion). Instead, we find that ridges and troughs are merging, diverging, or even folding concordantly (Figure 2b).

Based on these observations, we suggest that the mapped features are parts of a single structural system generated by distributed left-slip shear deformation. The cratered blocks are analogous to sigma clasts in ductile shear zones on Earth (Passchier, 1994; Passchier & Simpson, 1986; Simpson & Schmid, 1983). Left-slip shear deformation is indicated by the morphology of the cratered block sigma-clasts (Figure 4a), compressional folds (Figure 4b), and rotation of ridges toward a relic block indicating the sense of block rotation (Figure 4c). The sigma clast tails are most apparent for the easternmost block in the study area (Figure 4a). The orientation of the compressional structures (Figure 4b) indicate the left-lateral sense of shear. The

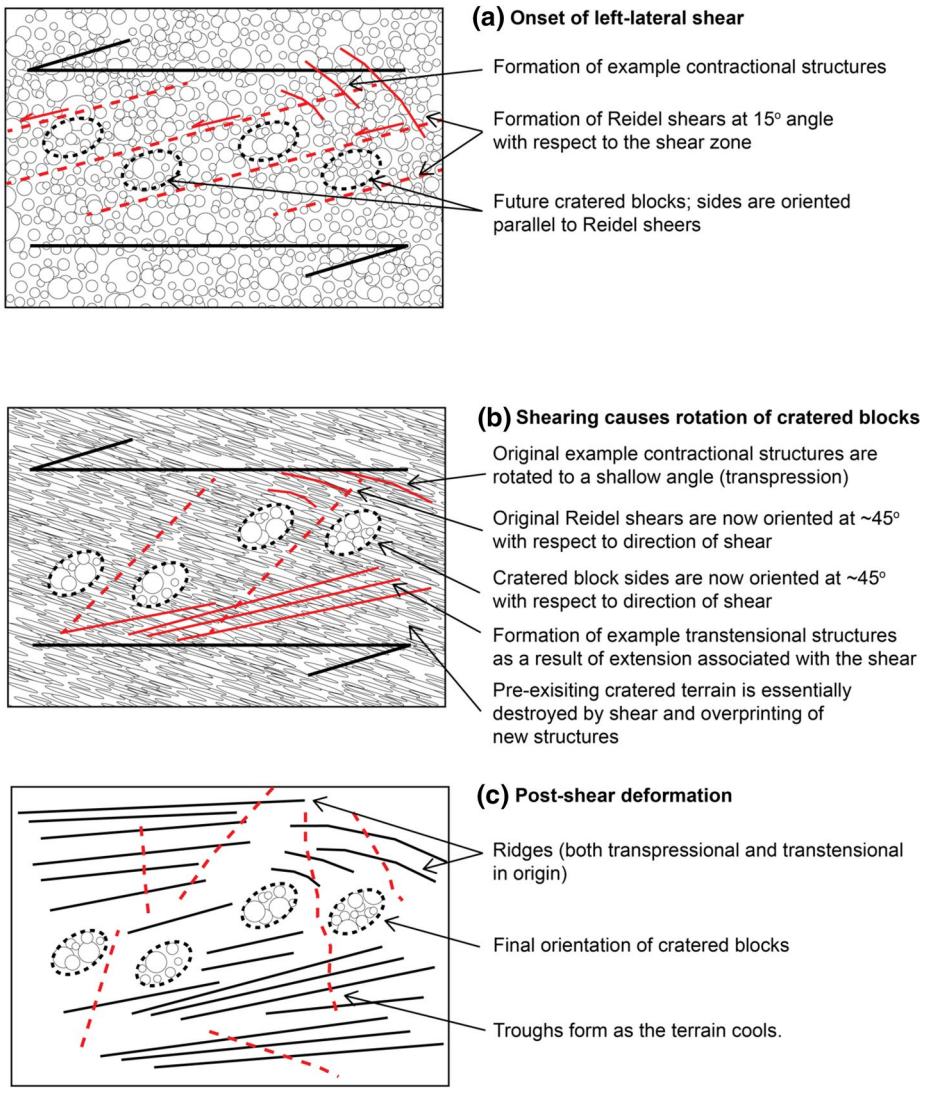

Figure 5. Block diagram of the proposed evolution of the relic cratered blocks. (a) The initial deformation of the terrain where left-lateral shear causes the formation of Riedel shear fractures (R-shears) at an angle of ~15° (α_o in Equation 1) with respect to the shear zone. (b) Block rotation and fragmentation accommodated by distributed slip along R-shears. Formation of transtensional structures as a result of extension associated with shearing. From analysis of the rigid cratered blocks, we find that they have rotated from an initial 15° orientation to ~ 45° (α in Equation 1) implying 30° of rotation. In order to achieve 30° of rotation, the shear zone must undergo ~70° of angular shear (γ in Equation 1). (c) Final orientation of the ridges and relic blocks. Cross-cutting troughs form, potentially from cooling of the terrain.

strain-shadow regions of the rotated blocks created local extension, which in turn caused inward warping of foliation and progressive tightening of ridges toward the rotated block (Figure 4c).

The kinematic development of the distributed left-slip shear zone is conceptualized in Figure 5. Specifically, we propose that the coherent cratered terrain was broken up by Riedel shears—strike-slip faults that form at a 15° angle to the shear zone—at the onset of left-lateral shearing and compressional features start to form. The cratered blocks form with a long axis quasiparallel to the Riedel shears (Figure 5a). As the left-lateral shearing of the terrain continues, the cratered blocks rotate counter-clockwize. Extensional structures form at a shallow angle with respect to the orientation of shear as a result of trans tension associated with the shear. The original contractional structures are now rotated to a shallow angle (Figure 5b). Then, the rotation of the ridges and cratered blocks ceases when the shearing ceases (Figure 5c). The formation of

Table 2
Corresponding Values for Each Variable and Quantity Calculated in Equations 1–4

Quantity	Value
α_0, initial orientation of blocks	15°
α, average final orientation of blocks [individual measurements]	45° [46°, 45°, 49°, 39°, 41°, 47°, 47°, 45°]
γ, angular shear	70°
ε, shear strain	2.8
T_{surf}, effective surface temperature[a]	70 K
σ, stress[a]	10 kPa^{-1} MPa
T_{bot}, temperature at base of deforming layer	190 K
μ, frictional coefficient[a]	0.5
ρ, density[a]	960 kg/m^3
g, gravitational acceleration[a]	0.113 m/s^2
k, thermal conductivity[a]	4.3 W/m/K

[a]See text for references on this quantity.

the contractional and extensional structures (see Figure 5b) during this time are responsible for erasing the craters in ductilely deformed regions surrounding the little deformed relic blocks of the Cratered Terrain.

4. Simple Quantitative Model and Results

Using a simplified analytical model, we can quantify our observations in the context of rheology and thermal state of Enceladus's ice shell during the deformation of the LHT. We estimate the finite strain from the rotated blocks, the thickness of the brittle ice shell, and the corresponding heat flux.

4.1. Strain Associated with Deformation

Following Fossen and Cavalcante (2017), the strain measured from the rotated blocks can be obtained by

$$\varepsilon = \cot(\alpha_0) - \cot(\alpha) = \tan(\gamma), \quad (1)$$

where ε is the strain, α_0 is the initial orientation of the rotated blocks, α is the final orientation of the rotated blocks, and γ is the angle, or amount, of shear. We assume that the deformation is homogeneous, which implies that the rotation angle can be derived from a passive marker—in this case, deflected ridges in the stress shadow region. This angle ranges from 39° to 49° near the eastern-most block (around 30°S, 280°E). All the measured values are recorded in Table 2, with the average being 45°. From the original 15° orientation of the ridges (assumed, see Figure 5), to rotate the blocks an additional 30° implies a total 70° of shear (γ), resulting in a strain of ~2.8. This is a first-order estimate of the strain involved in deforming this terrain. The deformation could be heterogeneous, resulting in the strain being unequally distributed across the region. However, since the entire region appears to have undergone distributed left-lateral shear, calculating the total strain of the whole region likely averages out any errors introduced by local heterogeneous deformation.

We can calculate the average strain rate using $\dot{\varepsilon} = \frac{\varepsilon}{\Delta t}$, where $\boldsymbol{\varepsilon}$ is the strain that we just calculated and Δt is the duration of formation. Thus, in order to estimate the average strain rate associated with the development of the shear zone, we need to estimate the duration of deformation. The crater-based age for the development of the LHT is estimated to be ~10 Ma (Crow-Willard & Pappalardo, 2015; Spencer & Nimmo, 2013), though this is highly uncertain (Kirchoff et al., 2018). However, the duration of formation is not equivalent to the age of the terrain, so this does not really provide a constraint on the duration of formation. Because the region lacks deformed craters which are apparent in other regions on Enceladus (e.g., Crow-Willard & Pappalardo, 2015), the deformation is not currently ongoing which means that the duration of deformation is less than the age of Enceladus or, ~4 Gy. By using this maximum duration for the formation, we find the

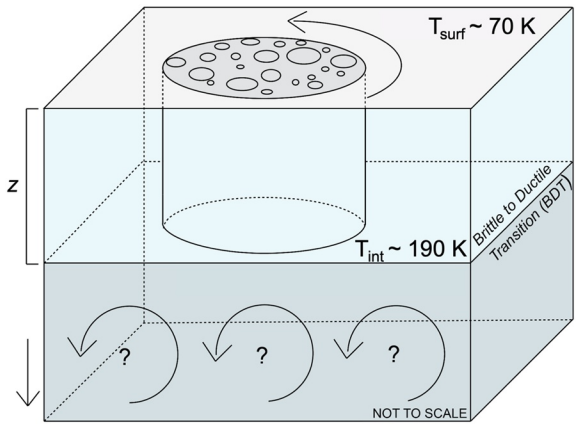

Figure 6. Block diagram of the relic cratered terrain and associated subsurface. The top layer, indicated by z, is the layer in which the relic cratered terrain is embedded, where z is the thickness of that layer. The bottom layer represents the ductile ice, which is potentially convecting.

minimum average strain rate to be $\sim 10^{-17}$ s^{-1}. The strain rate is likely higher than this, perhaps more on the order of $\sim 10^{-13}$ s^{-1}, which would be the case if the duration of formation was $\sim$ 1 My. Without a better constraint on the duration of deformation we can only speculate and calculate the minimum average strain rate of 10^{-17} s^{-1}.

4.2. Estimated Heat Flux

The ductile deformation of the ice, expressed as curvilinear ridge and rotation of the relic cratered blocks, is driven by the stress in the shear zone. The stress magnitude is estimated to be ~100 kPa, which is a mid-range stress magnitude generated by many hypothesized stress sources including warm-ice convection, diurnal tides, and gravitational spreading of uneven ice-shell thickness under thermal perturbation (e.g., Hurford et al., 2007; O'Neill & Nimmo, 2010; Smith-Konter & Pappalardo, 2008; Yin et al., 2016). We will explore alternative stress mechanisms in Section 5.2.

We require that the stress be equal to the frictional shear stress on the boundary of the brittle cratered blocks because this is implied by the failure we observe in this area when the blocks rotated. The vertically averaged frictional shear stress, σ can be estimated by:

$$\sigma = \frac{1}{z}\int_0^z \left(\mu\rho g z'\right) dz' = \frac{1}{2}\mu\rho g z, \tag{2}$$

where z is the brittle ice thickness (see Figure 6), μ is the frictional coefficient for ice, ρ is the density, and g is the gravitational acceleration on Enceladus. Thus, we estimate the brittle ice-shell thickness by

$$z = \frac{2\sigma}{\mu\rho g} \tag{3}$$

Using an experimentally determined value of friction coefficient of μ ~0.5 for ice (Dempsey, 2000; Dempsey et al., 1999; Schulson & Fortt, 2012) and assuming that σ is on the order of 100 kPa, we find that $z \sim 4$ km. We list all the model parameters in Table 2.

From the average interior temperature obtained from Equation 3 and the brittle ice-shell thickness determined in Equation 3, we obtain the heat flux F during the shear-zone development from the following relationship after Petrenko and Whitworth (1999):

$$F = \frac{k\left(T_{\text{surf}} - T_{\text{int}}\right)}{z}, \tag{4}$$

where k is the thermal conductivity, T_{surf} is the temperature of the surface, and T_{int} is the temperature at the base of the brittle layer. We then calculate the heat flux from Equation 4 by taking the surface temperature, T_{surf}, to be ~70 K (e.g., O'Neill & Nimmo, 2010), and the temperature at the brittle-to-ductile transition, T_{int}, to be ~190 K (though T_{int} is not well known, this value is in the range typically used, e.g. Barr & Hammond, 2015) resulting in a surface heat flux of ~0.13 W/m^2. This calculation assumes a constant thermal conductivity throughout the deforming ice shell. Including a temperature dependent thermal conductivity will increase the resulting heat flux, because as the temperature decreases, the conductivity increases.

5. Discussion

The formation of the relic cratered terrain in a regional left-lateral shear zone has implications for the evolution of Enceladus including past heating events, or resurfacing history, and global tectonics. From the inferred stress mechanism and calculated brittle layer thickness (Equation 3; Table 2), we infer the heat flux in this region when the structures formed, or the paleo-heat flux (Equation 4). We also investigate relaxing

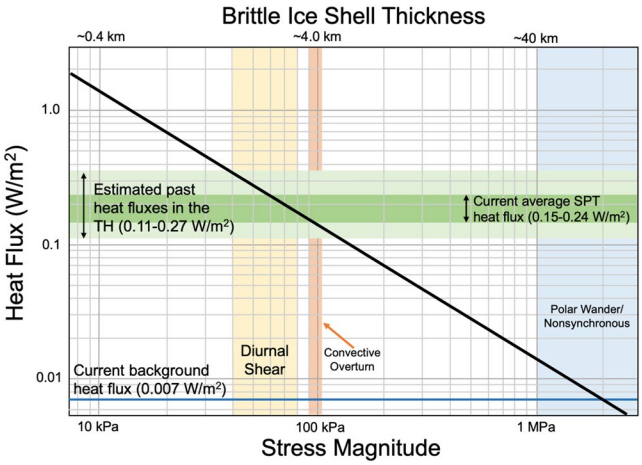

Figure 7. Plot of stress magnitude (bottom axis) or brittle ice shell thickness (top axis) versus heat flux. The black line represent the possible values of heat flux (Equation 4) given a stress magnitude or brittle ice shell thickness (Equation 3). The blue line indicates the current background heat flux from Enceladus's surface (Spencer & Nimmo, 2013). The colored boxes represent different estimated heat fluxes or stress magnitude ranges from other works. The dark green box is the range of measured current average South Polar Terrain (SPT) heat flux (Howett et al., 2011; Spencer et al., 2009; Spencer & Nimmo, 2013). The light green box are the calculated paleo heat fluxes for regions in the Trailing Hemisphere (TH) of Enceladus (Bland et al., 2007, 2012; Giese et al., 2008). The yellow box indicates an estimated range of maximum shear stresses generated by the diurnal cycle (e.g., Hurford et al., 2007). The orange box is the estimated average stresses generated by convective overturn (O'Neill & Nimmo, 2010). The blue box indicates possible stresses generated by nonsynchronous rotation (Patthoff et al., 2019) or polar wander (Nimmo & Pappalardo, 2006).

some of the assumptions that go in to the simple analytical model (e.g., stress mechanism and magnitude). Additionally, from a global perspective, we hypothesize that the regional left-lateral shear zone may extend around the Leading Hemisphere of Enceladus, possibly indicative of a hemispheric scale toroidal flow.

5.1. Deformation History of the Leading Hemisphere

Based on our analysis of the structures in the southern LHT, we find that the terrain likely formed due to regional left-lateral shear. The morphological evidence for left-lateral shear includes rotated cratered blocks, and the orientation of compressional and extensional features (Section 3). Further, evidence for the regional shear is the apparent lack of age relationships between the features identified in the mapping. The only age relationship apparent from relative cratering is that the terrain on the rotated blocks is older than the surrounding ridges terrain because the few craters mapped in the study area are concentrated exclusively on the surfaces of the relatively undeformed relic blocks. The only structures with evident cross-cutting relationships are the Fractures (major and minor), which cross-cut all the ridge structures, indicating that the Fractures are the youngest features in this region. The lack of other apparent cross-cutting structures in the map implies that the majority of the structures, mainly the sharp-crested and rounded-top ridges, formed contemporaneously. This widespread and contemporaneous regional deformation appears to favor an episodic deformation history for Enceladus. If the resurfacing on the LHT was part of a monotonic evolution of surface deformation, we would expect to see cross-cutting relationships that indicate the different eras or resurfacing.

5.2. Paleo-Heat Flux

Based on our calculations, described in Section 4, the relic cratered terrain formed at a time when the heat flux measured from the surface was ~ 0.13 W/m^2. This falls near the range of heat fluxes measured at the SPT today (from IR measurements), 0.15–0.24 W/m^2 (Howett et al., 2011; Spencer et al., 2009; Spencer & Nimmo, 2013), the range of paleo-heat fluxes (0.1–0.27+ W/m^2) calculated by previous work in other places on Enceladus (Bland et al., 2007, 2012; Giese et al., 2008), and that is predicted by resurfacing models (e.g., O'Neill & Nimmo, 2010; Barr & Hammond, 2015; Figure 7). The mechanisms to produce the heat flux emitting from the SPT today are debated (e.g., Behounkova et al., 2012; Mitri & Showman, 2008; O'Neill & Nimmo, 2010; Roberts & Nimmo, 2008; Shoji et al., 2013), and cannot easily reproduce the heat flux observed in the SPT. Thus, while it appears that the observations and calculations in this study as well as other recent studies (e.g., Bland et al., 2012, 2007; Giese et al., 2008) find a high heat flux was required in the past, a high paleo-feat flux is difficult to justify without a mechanism to produce the currently observed heat flux measured in the SPT.

Our estimated value for the heat flux at the time of terrain formation heavily depends on the magnitude of stress invoked. In Section 4, we use a stress value of 100 kPa because it is the high-end of diurnal shear stresses known to act on Enceladus (Figure 7). However, there are more exotic stress mechanisms that could generate larger stresses on Enceladus, resulting in a lower heat flux. If, for example, global reorientation is responsible for the deformation, the stresses may exceed 1 MPa (Nimmo & Pappalardo, 2006). Additionally, there is tentative evidence for nonsynchronous rotation (NSR) of Enceladus's ice shell (Patthoff & Kattenhorn, 2011) and the stress magnitude generated could be > 1 MPa (Patthoff et al., 2019). If NSR or polar wander is the responsible mechanism for creating this terrain, then the heat flux would potentially not need to be elevated above the current background (Figure 7). Because we cannot further constrain the stress magnitude, all we can say is that the southern LHT either formed with an elevated heat flux (similar to that which is measured in the SPT today) or under stresses that exceed 1 MPa (such as due to ice shell reorientation).

5.3. Hemispheric-Scale Toroidal Flow

Incorporating the idea that the southern leading hemisphere formed in response to a left-lateral shear zone into the broader global context, we propose that the leading hemisphere has experienced toroidal flow. Hemispheric clockwise toroidal flow could be responsible for the southern left lateral shear zone and the apparent circular feature that dominates the hemisphere (Figure 1). The plausibility of this large-scale toroidal flow could be investigated further with future detailed mapping of the remainder of the leading hemisphere. There is new evidence suggesting that the SPT could have also formed under this sort of toroidal flow (Schoenfeld & Yin, 2018), but the work is preliminary. The source of the potential toroidal flow is unknown but could be related to the orbital mechanics of the moon and the dissipation of energy into the ice shell and ocean. Other formation mechanisms are possible for the identified regional left-lateral shear zone, but have yet to be identified.

6. Conclusions

In this work, we produce a structural map of the Enceladus' southern LHT. We find that this region, defined by the presence of the unique cratered blocks, was likely formed in a regional left-lateral shear zone. We compare the deformation to the analog scenario of rotated clasts in shear zone's on Earth. We calculate a strain of ~2.8 associated with the deformation and a minimum strain rate of 10^{-17} s^{-1} and note that the strain rate is likely significantly larger. The mapping reveals a lack of relative age relationships among the identified ridges, indicating that the majority of deformation occurred concordantly. This short-lived and concordant deformation supports an episodic history of resurfacing on Enceladus. Based on our calculations, we propose that the resurfacing event that formed the LHT could have resulted from a heat flux similar to that currently in the SPT, if diurnal or convective stresses are responsible for deformation, or a stress mechanism that resulted in stresses > 1 MPa (such as ice shell reorientation).

The orientation of the shear zone and its apparent continuation around the remainder of the Leading Hemisphere may indicate that it was driven by clockwise toroidal flow in the ductile subsurface ice. The origin of this possible hemispheric-scale flow is beyond the scope of this work, and its plausibility could be explored further in future detailed mapping of the entire LHT and physical analog modeling work. However, this potentially high-heat, ductile resurfacing event in the LHT has implications for the formation of the SPT, the episodic nature of Enceladus resurfacing, and the dynamics and rheology of the ice shell.

Data Availability Statement

Images of Enceladus are from the Cassini ISS and are available in NASA PDS (https://pds-imaging.jpl.nasa.gov/search/?fq=-ATLAS_THUMBNAIL_URL%3Abrwsnotavail.jpg&fq=ATLAS_MISSION_NAME%3Acassini&fq=ATLAS_INSTRUMENT_NAME%3Aiss&fq=TARGET%3Aenceladus&q=*%3A*).

Or for the processed versions, see the global basemap from the USGS (https://astrogeology.usgs.gov/search/map/Enceladus/Cassini/Enceladus_Cassini_ISS_Global_Mosaic_100m_HPF). The measurements of the final orientation of the blocks (ridge orientation in the strain shadow near listed in Table 2 were taken in ArcGIS in Mercator projection (in order to preserve angles), but the mapping was performed in Adobe Illustrator.

Acknowledgments
This work was supported by the Furukawa Memorial Fellowship at UCLA and by NASA Headquarters under the NASA Earth and Space Science Fellowship Program – Grant 80NSSC17K0602. Portions of this research were carried out at the Jet Propulsion Laboratory, California Institute of Technology, under contract with the National Aeronautics and Space Administration.

References

Barr, A. C., & Hammond, N. P. (2015). A common origin for ridge-and-trough terrain on icy satellites by Sluggish lid convection. *Physics of the Earth and Planetary Interiors*, *249*, 18–27. https://doi.org/10.1016/j.pepi.2015.09.009

Barr, A. C., & Preuss, L. J. (2010). On the origin of south polar folds on Enceladus. *Icarus*, *208*, 499503. https://doi.org/10.1016/j.icarus.2010.03.038

Bland, M. T., Beyer, R. A., & Showman, A. P. (2007). Unstable extension of Enceladus lithosphere. *Icarus*, *192*, 92–105. https://doi.org/10.1016/j.icarus.2007.06.011

Bland, M. T., McKinnon, W. B., & Schenk, P. M. (2015). Constraining the heat flux between Enceladus' tiger stripes: Numerical modeling of funicular plains formation. *Icarus*, *260*, 232–245. https://doi.org/10.1016/j.icarus.2015.07.016

Bland, M. T., Singer, K. N., Mckinnon, W. B., & Schenk, P. M. (2012). Enceladus' extreme heat flux as revealed by its relaxed craters. *Geophysical Research Letters*, *39*, 1–5. https://doi.org/10.1029/2012GL052736

Burbank, D. W., & Anderson, R. S. (2009). *Tectonic geomorphology*. John Wiley & Sons.
Běhounková, M., Tobie, G., Choblet, G., & Čadek, O. (2012). Tidally-induced melting events as the origin of south-pole activity on Enceladus. *Icarus*, *219*, 655–664. https://doi.org/10.1016/j.icarus.2012.03.024
Crow-Willard, E. N., & Pappalardo, R. T. (2015). Structural mapping of Enceladus and implications for formation of teutonized regions. *Journal of Geophysical Research: Planets*, *120*, 928–950. https://doi.org/10.1002/2015JE004818
Dempsey, J. P. (2000). Research trends in ice mechanics. *International Journal of Solids and Structures*, *37*(1), 131–153.
Dempsey, J. P., Adamson, R. M., & Mulmule, S. V. (1999). Scale effects on the in-situ tensile strength and fracture of ice. Part II: First-year sea ice at resolute, NWT. *International Journal of Fracture*, *95*(1–4), 347–366.
Fossen, H., & Cavalcante, G. C. G. (2017). Shear zones–A review. *Earth-Science Reviews*, *171*, 434–455.
Gall, L., Leyrat, C., Janssen, M., Choblet, G., tobie, G., Bourgeois, O., et al. (2017). Thermally anomalous features in the subsurface of enceladus's south polar terrain. *Nature Astronomy*, *1*(4), 1–5. https://doi.org/10.1038/s41550-017-0063
Giese, B., Wagner, R., Hussmann, H., Neukum, G., Perry, J., Helfenstein, P., & Thomas, P. C. (2008). Enceladus: An estimate of heat flux and lithospheric thickness from flexurally supported topography. *Geophysical Research Letters*, *35*, 1–5. https://doi.org/10.1029/2008GL036149
Han, L., Tobie, G., & Showman, A. P. (2012). The impact of a weak south pole on thermal convection in Enceladus' ice shell. *Icarus*, *218*, 320–330. https://doi.org/10.1016/j.icarus.2011.12.006
Howett, C. J. A., Spencer, J. R., Pearl, J., & Segura, M. (2011). High heat flow from Enceladus' south polar region measured using 10–600 cm^{-1} Cassini/CIRS data. *Journal of Geophysical Research*, *116*(E3), E03003. https://doi.org/10.1029/2010JE003718
Hurford, T. A., Helfenstein, P., Hoppa, G. V., Greenberg, R., & Bills, B. G. (2007). Eruptions arising from tidally controlled periodic openings of rifts on Enceladus. *Nature*, *447*, 292–294. https://doi.org/10.1038/nature05821
Kirchoff, M. R., Bierhaus, E. B., Dones, L., Robbins, S. J., Singer, K. N., Wagner, R. J., & Zahnle, K. J. (2018). Cratering histories in the saturnian system. In *Enceladus and the icy moons of Saturn, Space science series* (pp. 267–284). Tucson, AZ: The University of Arizona Press.
Leonard, E. J., Pappalardo, R. T., & Yin, A. (2018). Analysis of very-high-resolution Galileo images and implications for resurfacing mechanisms on Europa. *Icarus*, *312*, 100–120. https://doi.org/10.1016/j.icarus.2018.04.016
Lucchetti, A., Pozzobon, R., Mazzarini, F., Cremonese, G., & Massironi, M. (2017). Brittle ice shell thickness of Enceladus from fracture distribution analysis. *Icarus*, *297*, 252–264. https://doi.org/10.1016/j.icarus.2017.07.009
Martin, E. S., Kattenhorn, S. A., Collins, G. C., Michaud, R. L., Pappalardo, R. T., & Wyrick, D. Y. (2017). Pit chains on Enceladus signal the recent tectonic dissection of the ancient cratered terrains. *Icarus*, *294*, 209–217. https://doi.org/10.1016/j.icarus.2017.03.014
Mitri, G., & Showman, A. P. (2008). A model for the temperature-dependence of tidal dissipation in convective plumes on icy satellites: Implications for Europa and Enceladus. *Icarus*, *195*, 758–764. https://doi.org/10.1016/j.icarus.2008.01.010
Moore, J. M., Asphaug, E., Morrison, D., Spencer, J. R., Chapman, C. R., Bierhaus, B., et al. (1999). Mass movement and landform degradation on the icy Galilean satellites: Results of the Galileo nominal mission. *Icarus*, *140*, 294–312.
Moore, J. M., Black, G., Buratti, B., Phillips, C. B., Spencer, J., & Sullivan, R. (2009). *Surface properties, regolith, and landscape degradation* (p. 329349). Tucson, Az: University of Arizona Press.
Nimmo, F., & Pappalardo, R. T. (2006). Diapir-induced reorientation of Saturn's moon Enceladus. *Nature*, *441*(7093), 614–616. https://doi.org/10.1038/nature04821
O'Neill, C., & Nimmo, F. (2010). The role of episodic overturn in generating the surface geology and heat flow on Enceladus. *Nature Geoscience*, *3*, 88–91. https://doi.org/10.1038/ngeo731
Paranicas, C., Roussos, E., Krupp, N., Kollmann, P., Hendrix, A. R., Cassidy, T., et al. (2012). Energetic charged particle weathering of Saturn's inner satellites. *Planetary and Space Science*, *61*(1), 60–65.
Passchier, C. W. (1994). Mixing in flow perturbations: A model for development of mantled porphyroclasts in mylonite. *Journal of Structural Geology*, *16*(5), 733–736.
Passchier, C. W., & Simpson, C. (1986). Porphyroclast systems as kinematic indicators. *Journal of Structural Geology*, *8*(8), 831–843.
Patterson, G. W., Collins, G. C., Head, J. W., Pappalardo, R. T., Prockter, L. M., Lucchitta, B. K., & Kay, J. P. (2010). Global geological mapping of Ganymede. *Icarus*, *207*(2), 845–867.
Patthoff, D. A., & Kattenhorn, S. A. (2011). A fracture history on Enceladus provides evidence for a global ocean. *Geophysical Research Letters*, *38*(18), L18201. https://doi.org/10.1029/2011GL048387
Patthoff, D. A., Kattenhorn, S. A., & Cooper, C. M. (2019). Implications of nonsynchronous rotation on the deformational history and ice shell properties in the south polar terrain of Enceladus. *Icarus 321*. https://doi.org/10.1016/J.ICARUS.2018.11.028
Patthoff, D. A., Pappalardo, R. T., Chilton, H. T., Thomas, T., & Schenk, P. (2015). Diverse origins of Enceladus's ridge terrains including evidence for contraction. Lunar and planetary science conference (Vol. 46, (2870). LPI.
Petrenko, V. F., & Whitworth, R. W. (1999). *Physics of ice*. Oxford, UK: Oxford University Press.
Porco, C. C. (2006). Cassini Observes the Active South Pole of Enceladus. *Science*, *311*(5766), 1393–1401. https://doi.org/10.1126/science.1123013
Porco, C., DiNino, D., & Nimmo, F. (2014). How the geysers, tidal stresses, and thermal emission across the south polar terrain of Enceladus are related. *The Astronomical Journal*, *148*, 45. https://doi.org/10.1088/0004-6256/148/3/45
Prockter, L. M., Figueredo, P. H., Pappalardo, R. T., Head, J. W., & Collins, G. C. (2000). Geology and mapping of dark terrain on Ganymede and implications for grooved terrain formation. *Journal of Geophysical Research*, *105*(E9), 22519–22540.
Prockter, L. M., Head, J. W., Pappalardo, R. T., Sullivan, R. J., Clifton, A. E., Giese, B., & Neukum, G. (2002). Morphology of European bands at high resolution: A mid-ocean ridge-type rift mechanism. *Journal of Geophysical Research*, *107*(E5). https://doi.org/10.1029/2000JE001458
Roberts, J. H., & Nimmo, F. (2008). Near-surface heating on Enceladus and the south polar thermal anomaly. *Geophysical Research Letters*, *35*(9), https://doi.org/10.1029/2008gl033725
Schoenfeld, A. M., & Yin, A. (2018). First tectonic stress map across Enceladus' SPT and possible dynamic causes. GSA Annual Meeting in Indianapolis, Indiana, USA-2018. GSA.
Schulson, E. M., & Fortt, A. L. (2012). Friction of ice on ice. *Journal of Geophysical Research*, *117*(B12), B12204. https://doi.org/10.1029/2012JB009219
Shoji, D., Hussmann, H., Kurita, K., & Sohl, F. (2013). Ice rheology and tidal heating of Enceladus. *Icarus*, *226*(1), 10–19. https://doi.org/10.1016/j.icarus.2013.05.004
Sieveka, E. M., & Johnson, R. E. (1982). Thermal-and plasma-induced molecular redistribution on the icy satellites. *Icarus*, *51*(3), 528–548.
Simpson, C., & Schmid, S. M. (1983). An evaluation of criteria to deduce the sense of movement in sheared rocks. *The Geological Society of America Bulletin*, *94*(11), 1281–1288.

Smith-Konter, B., & Pappalardo, R. T. (2008). Tidally driven stress accumulation and shear failure of Enceladus's tiger stripes. *Icarus*, *198*, 435–451. https://doi.org/10.1016/j.icarus.2008.07.005

Spencer, J. R., Barr, A. C., Esposito, L. W., Helfenstein, P., Ingersoll, A. P., Jaumann, R., McKay, C. P., et al. (2009). Enceladus: An active cryovolcanic satellite. *Saturn from Cassini-Huygens* (pp. 683–724). https://doi.org/10.1007/978-1-4020-9217-6_21

Spencer, J. R., & Nimmo, F. (2013). Enceladus: An Active Ice World in the Saturn System. *Annual Review of Earth and Planetary Sciences*, *41*, 693–717. https://doi.org/10.1146/annurev-earth-050212-124025

Spitale, J. N., Hurford, T. A., Rhoden, A. R., Berkson, E. E., Platts, S. S. (2015). Curtain eruptions from Enceladus/' south-polar terrain. *Nature 521*, 57–60. https://doi.org/10.1038/nature14368

Yin, A., & Pappalardo, R. T. (2015). Gravitational spreading, bookshelf faulting, and tectonic evolution of the South Polar Terrain of Saturn's moon Enceladus. *Icarus*, *260*, 409–439. https://doi.org/10.1016/j.icarus.2015.07.017

Yin, A., Zuza, A. V., & Pappalardo, R. T. (2016). Mechanics of evenly spaced strike-slip faults and its implications for the formation of tiger-stripe fractures on Saturn's moon Enceladus. *Icarus*, *266*, 204–216